Proceedings of the ASME 2015 International Technical Conference and Exhibition on Packaging and Integration of Electronic and Photonic Microsystems and ASME 2015 13th International Conference on Nanochannels, Microchannels, and Minichannels
InterPACKICNMM2015
July 6-9, 2015, San Francisco, California, USA

InterPACKICNMM2015-48262

Tailoring of permeability in copper inverse opal for electronic cooling applications

Chi Zhang
Department of Mechanical Engineering Stanford University
Stanford, CA 94305

Guoguang Rong
Deparment of Micro/Nano-electronics
Shanghai Jiao Tong University
Shanghai, P.R.China

James W. Palko
Department of Mechanical Engineering Stanford University
Stanford, CA 94305

Thomas J. Dusseault
General Electric Global Research,
Niskayuna, NY 12309

Mehdi Asheghi
Department of Mechanical Engineering
Stanford University
Stanford, CA 94305

Juan G. Santiago
Department of Mechanical Engineering
Stanford University
Stanford, CA 94305

Kenneth E. Goodson
Department of Mechanical Engineering
Stanford University
Stanford, CA 94305

ABSTRACT
Microporous metals are extensively applied in convective cooling of high heat flux systems such as electronics. Traditional fabrication approaches, such as sintering of metallic particles, however, produce materials with limited fluid transport capability. Here, we demonstrate control and enhancement of the permeability of porous copper inverse opals produced via electrodeposition around a sacrificial polymer template. Sintering of the template is used to control the fluid transport network microstructure, with permeability increasing for increasing sintering times. These electrodeposited structures achieve permeabilities greater than 1×10^{-12} m^2 with 5 μm pores, roughly 5 times larger than those of porous sintered copper with comparable feature sizes. The high permeability and small feature sizes, with attendant high specific surface area and strong capillarity, offered by the sintered template electrodeposited copper are attractive for two phase cooling applications.

INTRODUCTION
Rising power densities across a number of industries have led to increasing interest in microporous metals for active and passive heat exchange technologies [1-3]. Their high surface area to volume ratio [4], high thermal conductivity [5] and high density of interconnected fluid-permeable pores [6] can potentially facilitate superior heat transfer. Porous metals are broadly used in electronics cooling applications ranging from heat pipes and vapor chambers to single phase convective enhancements [7-10]. Thermal and fluidic transport, characterized respectively by thermal conductivity and permeability, are key to the implementation of these materials in cooling applications.

In this work, we fabricated permeable copper inverse opal with a template-assisted method, as depicted in Figure 1. Copper is electrodeposited around a sacrificial template, which allows precise control of the resulting porous microstructure following template removal. Polystyrene spheres form the template considered here. Sintering of the template spheres is used to control the connecting throat diameter between adjacent pores. During the sintering process, the polymer spheres, which have a glass transition temperature of 100°C, are driven by surface tension to coalesce with adjacent particles and decrease their surface area, and consequently the volume of included voids, at elevated temperatures [11,12]. Although sluggish for large-size particles [13], sintering is reported to be more effective when polymer particles are as fine as several microns [11,14], due to larger surface to volume ratios. Sintering at temperatures above the glass transition temperature of polystyrene has also been reported to markedly accelerate the surface diffusion, resulting in dimensional changes [11].

Here we demonstrate the ability to tailor the fluid permeability of copper inverse opal with modification of the initial opal template by sintering processes. We characterize permeability of the resulting CIO structures using a flow geometry allowing measurements of thin films, which is particularly applicable to surface enhancement structures for boiling and evaporation. The effect of sintering time and temperature on the in-plane permeability is investigated. Scanning electron microscopy (SEM) of the copper inverse opal structures are analyzed to understand the dependence of permeability on sintering process parameters. We consider opportunities for application of copper inverse opals in two-phase cooling of electronics.

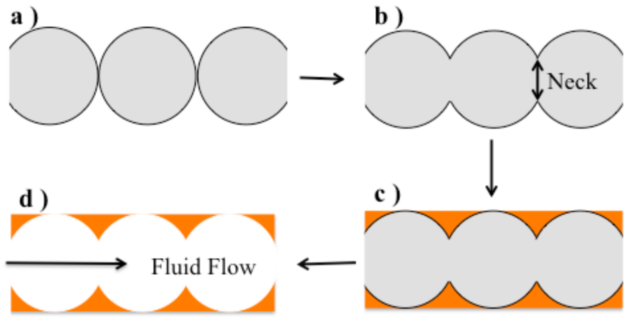

Figure 1. Schematic fabrication procedures of CIO with sintering modification of sacrificial templates. a) Polystyrene spheres are self-assembled using a drop casting method, creating point contacts between adjacent spheres. b) Necks between adjacent spheres are formed during the sintering process driven by surface tension, accompanied by template densification. c) Copper is electrodeposited around polystyrene templates. d) Removal of sacrificial templates results in permeable copper inverse opal structures.

SAMPLE PREPARATION

Inverse opal structures have been widely explored for various applications including photonic crystals [15-17], chemical sensors [18], solar cells [19,20], and supercapacitors [21]. The general fabrication procedure of inverse opals includes assembly of the sacrificial template and deposition of the interstitial material followed by dissolution the template leaving the inverse structure [17]. Polymer spheres are commonly used as sacrificial templates, the size of these ranging from tens of nanometers to several microns [21,22]. Different self-assembly methods like spin coating [23], sedimentation [21], drop casting [6,24], or Langmuir Blodgett [5,25] are selected based on desired periodicity, crystallinity, and geometry of the final structure. Filling of metals in the interstitials of templates has been demonstrated via electrodeposition [26] and chemical vapor deposition [27].

In this work, we prepared substrates for electrodeposition by sputtering a titanium adhesion layer (10nm) and a gold seed layer (50nm) on silicon wafers. The wafers were then cut into 2cm×2cm squares for each sample. The Ti/Au seed layers serve as the cathode for the copper electrodeposition. We synthesized polystyrene spheres of 5μm diameter using a dispersion polymerization method [28]. The polystyrene spheres are then self-assembled into random-packed templates on the substrate surface via a drop casting method [6].

We sintered the packed polystyrene beds at temperatures of 95°±0.5°C, 103°±0.5°C, and 110°±0.5°C in a conventional oven over a range of times. The temperature in the oven was monitored closely by thermocouples over the entire sintering duration. After the templates were cooled to ambient temperature, we wicked a small drop of ethanol into the hydrophobic polystyrene bed before immersing each sample in an aqueous electrolyte solution (0.6M $CuSO_4$ + 5mM H_2SO_4). We utilized a three-electrode PTFE electrolytic cell [5], which defines a 1cm×1cm electrodeposition area in the center of the substrates for porous metal growth. Potentiostatic electrodeposition was performed at a constant overpotential of 278 mV for 2400 seconds, with copper deposition starting from the Ti/Au seed layer of the substrate surface and continuing to fill the interstitials of the sintered templates. The above deposition process yielded copper inverse opal thin films of thickness 20±1μm, which is desirable for permeability measurements in this work.

PERMEABILITY CHARACTERIZATION

We designed a system for planar permeability measurements of thin films. Figure 2 shows a schematic and photographs of the measurement setup.

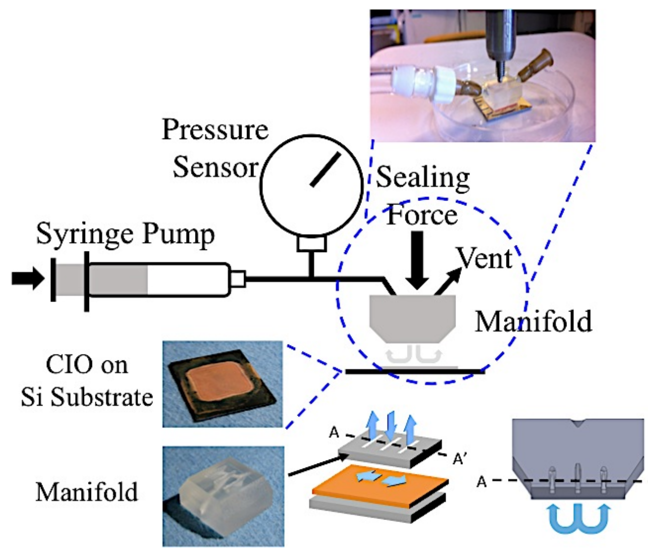

Figure 2. Experimental setup of planar permeability measurements. A syringe pump was used to drive air flow through the system. The pressure drop in the sample was measured with a pressure gauge just upstream of the sample, so that viscous pressure drop from the pressure gauge to the sample was negligible. The pressure downstream of the sample was assumed to be atmospheric.

We utilized a syringe pump to impose a fixed flow rate, and a pressure gauge to measure the resulting pressure difference between the inlet and outlet of the manifold. The manifold was manufactured with a 3D printing process, allowing rapid production of parts with features as fine as 16 μm. The 3D printed manifold consists of three slots symmetrically separated by 2.15mm, with the center one acting as inlet for the fluid flow, the other two as outlets. All three slots have dimensions of 6mm×1mm. A schematic of the nominal air flow path inside the inverse opal imposed by the manifold is shown in Figure 2.

The cross-linked acrylic resin used in the 3D printing process provides a good sealing surface when a pressure of 2.4×10^5 Pa normal to the measurement surface is applied. In addition, we maintain the temperature of the sealing surface at

49.5°±0.5°C by heating up the sample with a hot plate to further diminish leakages.

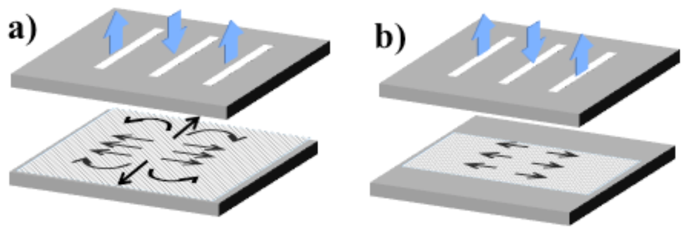

Figure 3. Edge effect characterization using post arrays microfabricated in silicon. a) The fluid domain (1cm×1cm) with edge effects is identical to the case of CIO samples. b) The fluid domain (6mm×1cm) has minimal edge effects, with the width of silicon micropost array fabricated to be the same as the length of inlet and outlet slots (6mm).

Not all flow occurs perpendicular to the inlet axis of the manifold. As shown in Figure 3a, a portion of the flow escapes directly from the inlet to the edge of the membrane and additional flow fringes from the end of the inlet to the outlets. This reduces the pressure drop associated with a given flow rate. We account for these effects by characterizing the pressure drops of two flow geometries, one larger allowing edge effects (Figure 3a) and one smaller allowing only flow perpendicular to the inlet axis (Figure 3b), for a lattice of silicon posts [29] at a given flow rate. The microfabricated posts considered here are 300μm in diameter, 30μm high, and 22μm apart. The non-permeable bulk silicon outside the region containing posts constrains flow to the microfabricated region. Preliminary results show that edge effects reduce permeability to 60.8% of its nominal value assuming only flow perpendicular to the inlet, and this scaling factor is applied to the CIO permeability calculations reported here.

Permeability is calculated from least square fits to the variation of pressure drop with inlet flow rate. We measured the steady pressure drop between the inlet and outlet of the manifold at a series of flow rates for each sample. According to Darcy's law, intrinsic permeability K of a porous medium is given by

$$Q = -\frac{KA}{\mu}\frac{(P_{out}-P_{in})}{L} \tag{1}$$

Here Q is the flow rate of air applied to the porous thin film, A is the cross-sectional area of the flow depending on the thickness of porous film, μ is the viscosity of air at the corresponding temperature, and L is the distance between inlet and outlet, over which the pressure drop takes place. A linear relationship of the pressure drop with respect to flow rate is shown in Figure 4, which validates our Darcy flow assumption.

RESULTS AND DISCUSSION

We examined the sintering effect on CIO permeability at temperatures of 95°±0.5°C, 103°±0.5°C, and 110°±0.5°C. Permeability is plotted as a function of sintering time for these sintering temperatures in Figure 5. The oven was held at 110°±0.5°C for 60 minutes, with samples removed every 10 minutes. Similarly, sintered samples were removed at intervals of 30 minutes for 103°±0.5°C, while sintering at 95°±0.5°C lasted for 12 hours, 18 hours, 24 hours, and 30 hours.

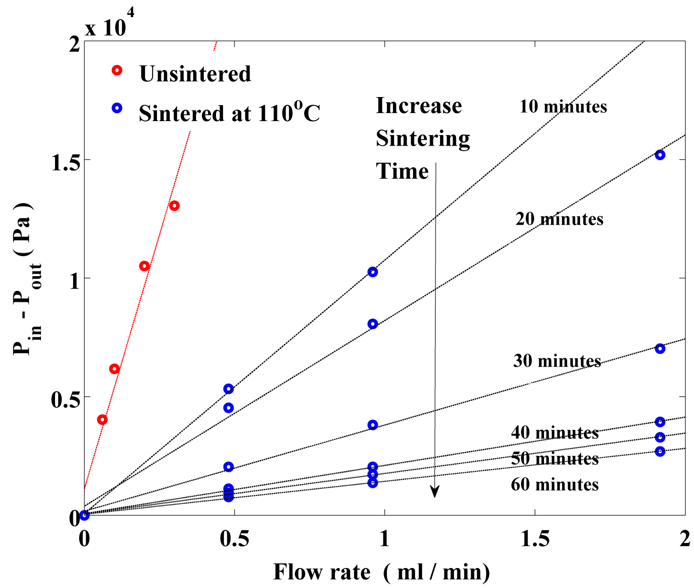

Figure 4. Pressure drop sustained by CIO samples at different flow rates. The slope of the linear fit represents $(P_{in} - P_{out})/Q$ in the permeability calculations.

Copper inverse opal thin film with no template sintering gives a permeability value on the order of 10^{-14}m^2, attributed to some random tortuous flow paths within the structure. This value could potentially be overestimated due to leakage of the experimental system, which plays a more significant role for less permeable samples. Sintering of the polystyrene template proves to be an effective approach to improve the permeability of the copper inverse opal thin films, with permeability values increasing up to two orders of magnitude. Sintering above the glass transition temperature of polystyrene (T_g=100°C) is found to markedly reduce the sintering time from days to minutes, promoting efficiency for tailoring the permeability. This is largely attributed to the significant increase of surface diffusion of polystyrene above T_g, which accelerates mass transport and boosts sphere coalescence.

The unsintered CIO sample in Figure 5(d) shows minimal interconnects between adjacent pores. During sintering, the neck diameter grows consistently with time (see Figure 5 insets), improving flow paths of the inverse opal structures. It should be noted that aggressive sintering at high temperatures, and/or for long durations could cause dimensional and compositional changes of the templates, such as pore shrinkage and gas evolution [11-12], which could lead to structural discontinuity of the inverse porous medium. More experiments need to be performed to determine the optimal sintering parameters.

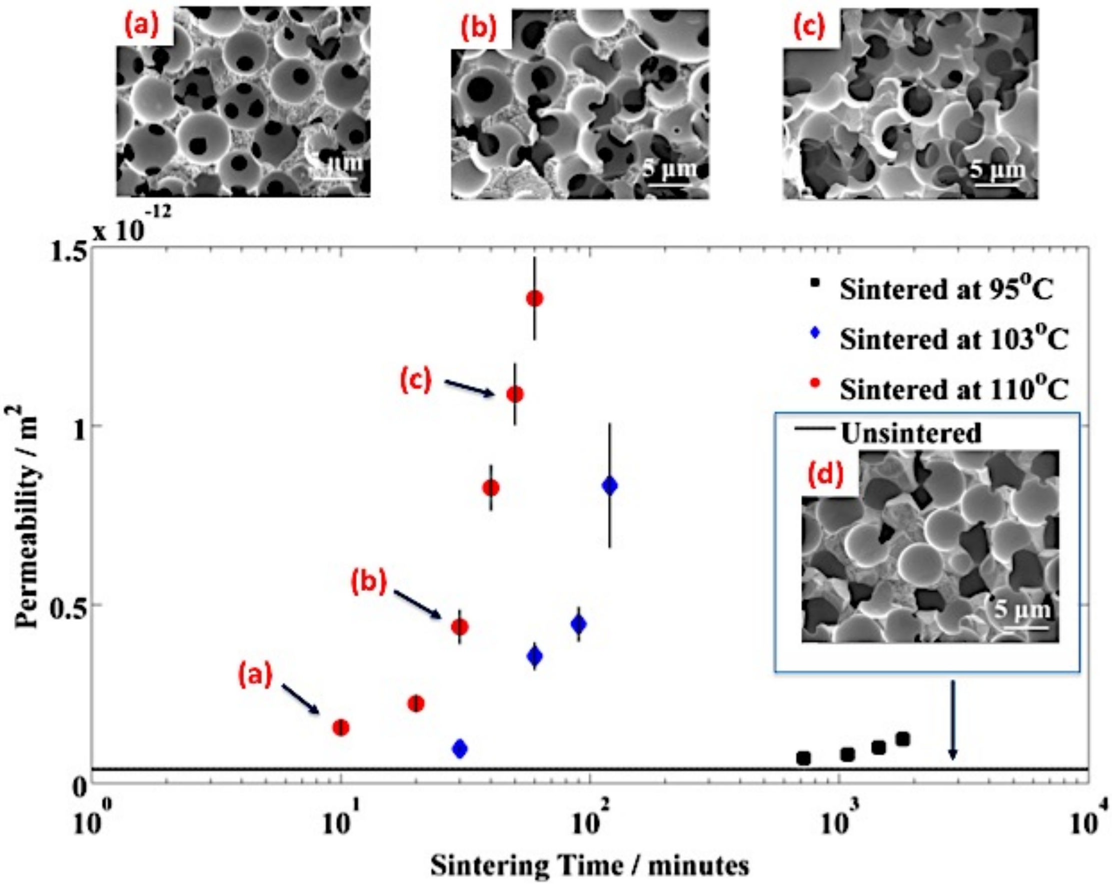

Figure 5. Results from permeability measurements as a function of isothermal sintering time for template-sintered CIO, including Scanning electron microscopy (SEM) images (inset) of samples a) sintered at 110°±0.5°C for 10 minutes, b) sintered at 110°± 0.5°C for 30 minutes, c) sintered at 110°±0.5°C for 50 minutes, and d) unsintered. Uncertainties in permeabilities of samples sintered at 110°±0.5°C and 103°±0.5°C are estimated based on 90% confidence intervals for the value of $(P_{in} - P_{out})/Q$ determined by linear regression (figure 4). Uncertainties based on pressure and flow rate for small permeability values (<3×10^{-13}m^2) are generally less than the symbol size.

Table 1. Characteristics of samples shown in Figure 5

Figure 5	Sintering Condition	Permeability K (m^2)	Neck Diameter d_n (μm)
(a)	110°±0.5°C 10 minutes	1.56×10^{-13}	1.8-2.1
(b)	110°±0.5°C 30 minutes	4.38×10^{-13}	2.6-2.9
(c)	110°±0.5°C 50 minutes	1.09×10^{-12}	3.2-3.6
(d)	Unsintered	4.01×10^{-14}	0

We compare our results with permeability measurements and calculations, as shown in Figure 6, for sintered copper, which is widely used as a porous wick for heat pipes and heat exchangers. In their recent paper, Dominguez Espinosa *et al.* [30] studied the effect of sintering on randomly packed copper particles, and showed that permeability only varied within a small range under different sintering conditions. Additionally, permeability did not show a clear trend with sintering time or temperature. It was concluded that permeability of sintered copper depends primarily on particle size, with average permeability increasing with particle size. Similar particle-size dependence is also evident in simulations performed for commercial sintered copper wicks in [31]. Figure 6 shows the expected (feature size)^2 dependence of permeability for sintered copper.

The achievable permeability of template-sintered CIO is seen to be significantly higher than that of sintered copper for comparable feature sizes. The surface to volume ratio and capillary suction of porous media scale inversely with feature size. The combination of high surface area, capillary suction, and permeability available with CIO is highly beneficial in two-phase electronic cooling applications. In contrast to sintered copper, template-sintered CIO also allows permeability to be tailored over a large range (e.g. from 4×10^{-14} to 1×10^{-12}m^2 as shown here) without a significant change in pore size based on template sintering conditions, as seen in Figure 5.

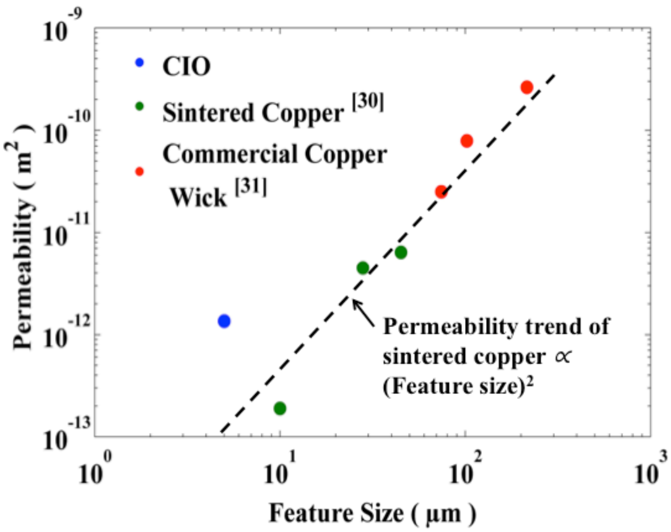

Figure 6. Permeability comparison between CIO and sintered copper powder wicks. Both experimentally measured permeability [30] and simulation results [31] are included for sintered copper. Feature size for CIO is denoted by the diameter of the opal template, while feature size for sintered copper is defined as copper particle size.

CONCLUSIONS

In this work, we demonstrate the ability to tailor the permeability of copper inverse opal thin films by varying the sintering process of the sacrificial template. This is an important step towards understanding the fluid flow within this microporous structure, and facilitating future design of one-phase or two-phase microfluidic heat exchangers for electronic cooling. Further work will be focused on revealing the relationship between permeability and porosity, which would provide insight into the convective heat transfer performance of these structures. This requires the ability to tune the porosity of microporous media within a reasonable range, either by modifying the self-assembly method of the template, or by varying the dimensions of the pores and interconnects. Further optimization of the template sintering process will also be explored.

ACKNOWLEDGEMENTS

The authors would like to thank Michael Barako for many helpful discussions. The authors are thankful for the support of the Defense Advanced Research Projects Agency ICECool Fundamentals program (agreement #HR0011-13-2-0011, “Phase Separation Diamond Microfluidics for HEMT Cooling”) and Chi Zhang would like to acknowledge support from Stanford University School of Engineering Graduate Fellowship. Guoguang Rong acknowledges support by Shanghai International Science and Technology Callaboration Program under Grant 13430710400.

NOMENCLATURE

Q	flow rate (m^3)
A	cross-section area (m^2)
P	pressure (Pa)
K	permeability (m^2)
L	distance between inlet and outlet (m)
d_n	neck diameter (μm)
T_g	glass transition temperature (K)

Greek Symbols

μ	dynamic viscosity (Pa s)

Subscripts

in	inlet of the flow geometry
out	outlet of the flow geometry
n	neck between adjacent spheres

REFERENCES

[1] Kim, J. H., S. M. You, and Stephen US Choi. "Evaporative spray cooling of plain and microporous coated surfaces." International Journal of Heat and Mass Transfer 47.14 (2004): 3307-3315.

[2] Xu, Jinliang, et al. "Pool boiling heat transfer of ultra-light copper foam with open cells." *International Journal of Multiphase Flow* 34.11 (2008): 1008-1022.

[3] Khodabandeh, Rahmatollah, and Richard Furberg. "Heat transfer, flow regime and instability of a nano-and micro-porous structure evaporator in a two-phase thermosyphon loop." *International journal of thermal sciences* 49.7 (2010): 1183-1192.

[4] J. Banhart, “Manufacture, characterization and application of cellular metals and metal foams”, Progress in Materials Science, vol. 46, no. 6, pp. 559–632, 2001.

[5] Barako, Michael T., et al. "Thermal conduction in nanoporous copper inverse opal films." *Thermal and Thermomechanical Phenomena in Electronic Systems (ITherm), 2014 IEEE Intersociety Conference on*. IEEE, 2014.

[6] Dusseault, Thomas J., et al. "Inverse opals for fluid delivery in electronics cooling systems." *Thermal and Thermomechanical Phenomena in Electronic Systems (ITherm), 2014 IEEE Intersociety Conference on*. IEEE, 2014.

[7] El-Genk, Mohamed S., and Amir F. Ali. "Enhanced nucleate boiling on copper micro-porous surfaces." *International Journal of Multiphase Flow* 36.10 (2010): 780-792.

[8] You, S. M. "Pool boiling heat transfer from plain and microporous, square pin-finned surfaces in saturated FC-72." (2000).

[9] Rainey, K. N., and S. M. You. "Effects of heater size and orientation on pool boiling heat transfer from microporous coated surfaces." *International Journal of Heat and Mass Transfer* 44.14 (2001): 2589-2599.

[10] Furberg, Richard. "Enhanced boiling heat transfer from a novel nanodendritic micro-porous copper structure." (2006).

[11] Jayaraman, Gowri Shankar, et al. "Cold compaction molding and sintering of polystyrene." *Polymer Engineering & Science* 16.8 (1976): 529-536.

[12] Greco, A., and A. Maffezzoli. "Polymer melting and polymer powder sintering by thermal analysis." *Journal of thermal analysis and calorimetry* 72.3 (2003): 1167-1174.

[13] Kuczynski, G. C., B. Neuville, and H. P. Toner. "Study of sintering of poly(methyl methacrylate)." *Journal of Applied Polymer Science* 14.8 (1970): 2069-2077.
[14] Mazur, S., R. Beckerbauer, and J. Buckholz. "Particle size limits for sintering polymer colloids without viscous flow." *Langmuir* 13.16 (1997): 4287-4294.
[15] Schroden, Rick C., et al. "Optical properties of inverse opal photonic crystals."*Chemistry of materials* 14.8 (2002): 3305-3315.
[16] Hatton, Benjamin, et al. "Assembly of large-area, highly ordered, crack-free inverse opal films." *Proceedings of the National Academy of Sciences* 107.23 (2010): 10354-10359.
[17] Waterhouse, Geoffrey IN, and Mark R. Waterland. "Opal and inverse opal photonic crystals: fabrication and characterization." *Polyhedron* 26.2 (2007): 356-368.
[18] Lee, Y ‐ J., and Paul V. Braun. "Tunable inverse opal hydrogel pH sensors." Advanced Materials 15.7 ‐ 8 (2003): 563-566.
[19] Su, Liap Tat, et al. "Photon Upconversion in Hetero ‐ nanostructured Photoanodes for Enhanced Near ‐ Infrared Light Harvesting." Advanced Materials 25.11 (2013): 1603-1607.
[20] Kwak, Eun Sik, et al. "Compact Inverse ‐ Opal Electrode Using Non ‐ Aggregated TiO2 Nanoparticles for Dye ‐ Sensitized Solar Cells." Advanced Functional Materials 19.7 (2009): 1093-1099.
[21] Kim, Jae-Hun, et al. "Ni–NiO core–shell inverse opal electrodes for supercapacitors." Chemical Communications 47.18 (2011): 5214-5216.
[22] Graugnard, Elton, et al. "Electric-field tuning of the Bragg peak in large-pore Ti O 2 inverse shell opals." Physical Review B 72.23 (2005): 233105.
[23] Kwak, Eun Sik, et al. "Compact Inverse ‐ Opal Electrode Using Non ‐ Aggregated TiO2 Nanoparticles for Dye ‐ Sensitized Solar Cells." Advanced Functional Materials 19.7 (2009): 1093-1099.
[24] Mandlmeier, Benjamin, et al. "Formation of interpenetrating hierarchical titania structures by confined synthesis in inverse opal." Journal of the American Chemical Society 133.43 (2011): 17274-17282.
[25] Mandlmeier, Benjamin, et al. "Formation of interpenetrating hierarchical titania structures by confined synthesis in inverse opal." Journal of the American Chemical Society 133.43 (2011): 17274-17282.
[26] Eagleton, Tom S., and Peter C. Searson. "Electrochemical synthesis of 3D ordered ferromagnetic nickel replicas using self-assembled colloidal crystal templates." Chemistry of materials 16.24 (2004): 5027-5032.
[27] Vlasov, Yurii A., et al. "On-chip natural assembly of silicon photonic bandgap crystals." Nature 414.6861 (2001): 289-293.
[28] Song, Jing-She, and Mitchell A. Winnik. "Cross-linked, monodisperse, micron-sized polystyrene particles by two-stage dispersion polymerization."*Macromolecules* 38.20 (2005): 8300-8307.
[29] Srivastava, Nimisha, et al. "A unified scaling model for flow through a lattice of microfabricated posts." *Lab on a Chip* 10.9 (2010): 1148-1152.
[30] Espinosa, FA Dominguez, T. B. Peters, and J. G. Brisson. "Effect of fabrication parameters on the thermophysical properties of sintered wicks for heat pipe applications." *International Journal of Heat and Mass Transfer* 55.25 (2012): 7471-7486.
[31] Bodla, Karthik K., Jayathi Y. Murthy, and Suresh V. Garimella. "Direct simulation of thermal transport through sintered wick microstructures." *Journal of heat transfer* 134.1 (2012): 012602.